Electronic Supplementary Material (ESI) for Journal of Materials Chemistry C.

Supporting Information

for

Layered Manganese Bismuth Tellurides with $GeBi_4Te_7$– and $GeBi_6Te_{10}$–type Structures: Towards Multifunctional Materials

Daniel Souchay,[†] Markus Nentwig,[†] Daniel Günther,[†] Simon Keilholz,[†] Johannes de Boor,[#] Alexander Zeugner,[‡] Anna Isaeva,[§§] Michael Ruck,[‡] Anja U. B. Wolter,[§] Bernd Büchner,[§,§§] Oliver Oeckler[†,*]

[†] Institute for Mineralogy, Crystallography and Materials Science; Faculty of Chemistry and Mineralogy, Leipzig University, Scharnhorststr. 20, 04275 Leipzig, Germany

Institute of Materials Research, German Aerospace Center, Linder Höhe, 51170 Cologne, Germany

[‡] Faculty of Chemistry and Food Chemistry, Technische Universität Dresden, 01062 Dresden, Germany

[§] Leibniz-Institute for Solid State and Materials Research, Helmholtzstr. 10, 01069 Dresden, Germany

[§§] Institute of Solid State Physics, Technische Universität Dresden, 01062 Dresden, Germany

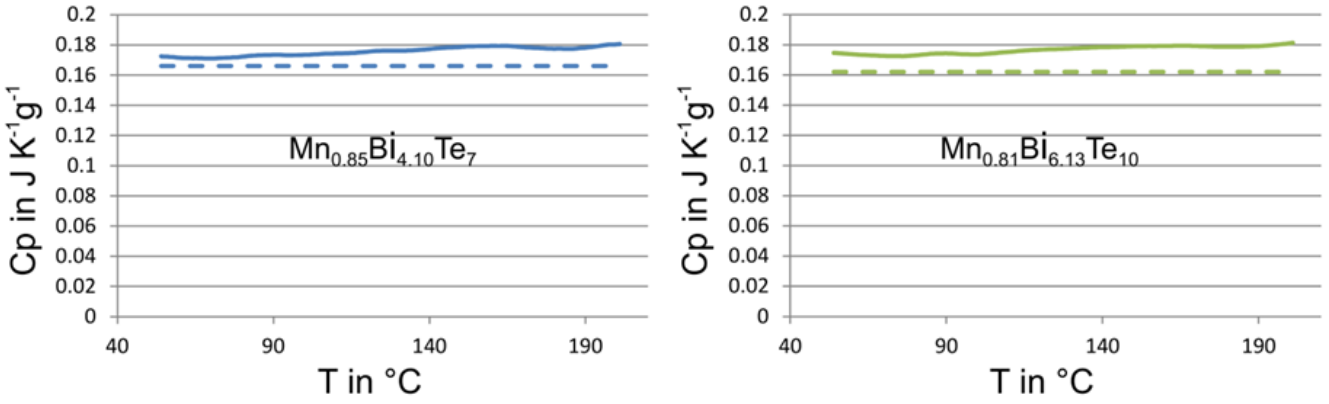

Figure S1: Heat capacity C_p determined by DSC measurements (Netzsch DSC 404, Pt crucibles with alumina inlays) for samples $Mn_{0.85}Bi_{4.10}Te_4$ (left) and $Mn_{0.81}Bi_{6.13}Te_{10}$ (right) as used for thermoelectric characterization and comparison with the Dulong-Petit approximation.

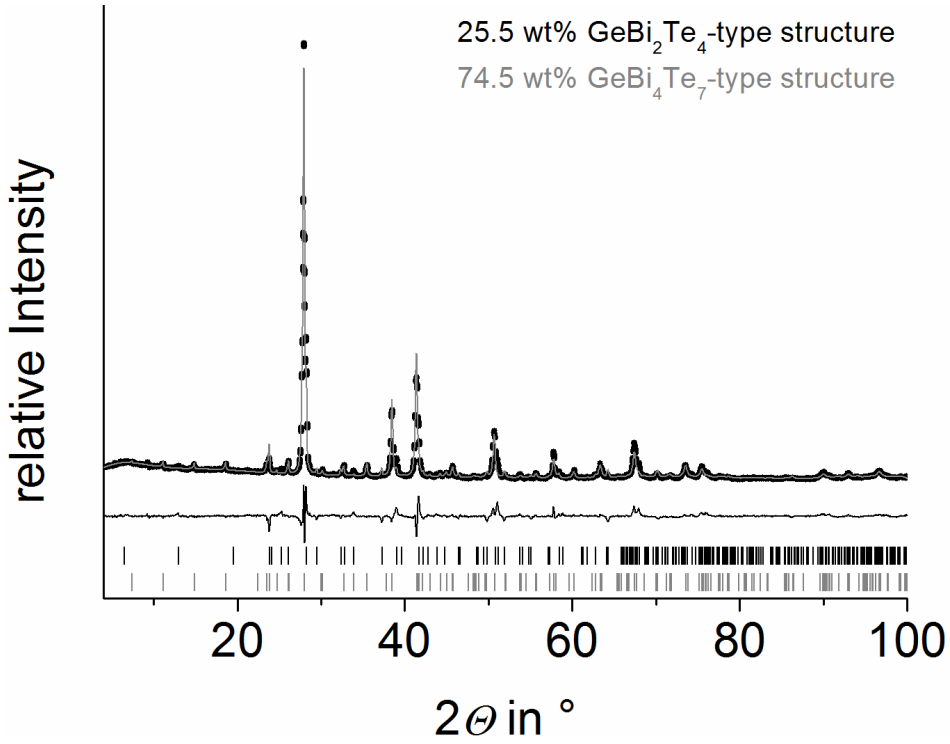

Figure S2: PXRD pattern of a sample with the nominal composition $MnBi_4Te_7$ (black points); Rietveld refinement taking into account structure models for $Mn_{0.85}Bi_{2.1}Te_4$ ($GeBi_2Te_4$-type structure) [Zeugner, A.; Nietschke, F.; Wolter A. U. B.; Gaß, S.; Vidal, R. C.; Peixoto, T. R. F.; Pohl, D.; Damm, C.; Lubk, A.; Hentrich, R.; Moser, S. K.; Fornari, C.; Min, C. H., Schatz, S.; Kißner, K.; Ünzelmann, M.; Kaiser, M.; Scaravaggi, F. Rellinghaus, B.; Nielsch, K.; Heß, C.; Büchner, B.; Reinert, F.; Bentmann, H.; Oeckler, O.; Doert, T.; Ruck, M.; Isaeva, A. Chemical Aspects of the Antiferromagnetic Topological Insulator $MnBi_2Te_4$; available at arxiv.org/abs/1812.03106] and $Mn_{0.85}Bi_{4.10}Te_7$ ($GeBi_4Te_7$-type structure) based on SCXRD refinements (see chapter 3.3), sum of calculated patterns light gray and experimental data black points; difference plot (black) and reflection markers (black lines $GeBi_2Te_4$-type structure, gray lines $GeBi_4Te_7$-type structure).

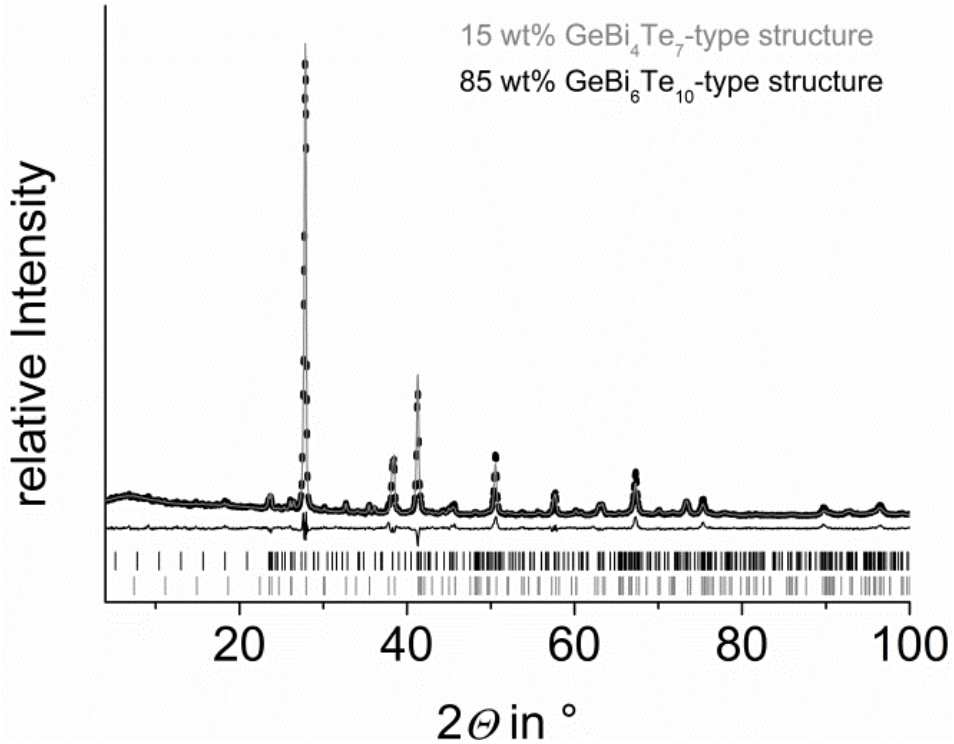

Figure S3: PXRD pattern of a sample with the nominal composition $MnBi_6Te_{10}$ (black points); Rietveld refinement taking into account structure models for $Mn_{0.85}Bi_{4.10}Te_7$ ($GeBi_4Te_7$-type structure) and $Mn_{0.73}Bi_{6.18}Te_{10}$ ($GeBi_6Te_{10}$-type structure) based on the SCXRD refinements (see chapter 3.3), sum of calculated patterns light gray and experimental data black points; difference plot (black) and reflection markers (black lines $GeBi_6Te_{10}$-type structure, gray lines $GeBi_4Te_7$-type structure).

Table S1: Details of the Rietveld refinements of samples with the nominal compositions $Mn_{0.85}Bi_{4.10}Te_7$ and $Mn_{0.81}Bi_{6.13}Te_{10}$ based on structure models for $Mn_{0.85}Bi_{4.1}Te_7$ ($GeBi_4Te_7$-type structure) and $Mn_{0.73}Bi_{6.18}Te_{10}$ ($GeBi_6Te_{10}$-type structure, the slightly different Mn content has no influence on the fit) from the SCXRD refinement (section 3.3).

formula	$Mn_{0.85}Bi_{4.10}Te_7$	$Mn_{0.73}Bi_{6.18}Te_{10}$
M (in g mol^{-1})	1796.715	7824.35
Z	1	3
F(000)	725.55	3154
crystal system	trigonal	trigonal
space group (no.)	$P\bar{3}m1$ (164)	$R\bar{3}m$ (166)
cell parameter (in Å)	a = 4.3613(1) c = 23.794(2)	a = 4.3694(2) c = 101.870(7)
cell volume (in Å^3)	391.95(3)	1674.3(2)
X-ray density (in g cm^{-3})	7.61	7.71
radiation	Cu-$K_{\alpha1}$ (λ = 1.540596 Å)	
2θ range (in °)	$4 \leq 2\theta \leq 100$	
number of reflections	216	310
refined parameter / thereof background	27 / 18	27 / 18
R_p / R_{wp}	0.0172 / 0.0269	0.0171 / 0.0264
R_{Bragg}	0.021	0.021
GooF	1.01	1.01

Table S2: Wyckoff positions and atomic parameters (coordinates *x y z*, site occupancy factors *s.o.f.* and isotropic displacement parameters B_{eq}, all from single-crystal data and not further refined) used in the Rietveld refinement of $Mn_{0.85}Bi_{4.10}Te_7$.

Atom	**Wyckoff**	***x***	***y***	***z***	***s. o. f.***	B_{eq}
Mn1 / Bi1 / □	1*b*	0	0	1/2	0.694 / 0.255 / 0.051	2.58
Mn2 / Bi2	2*d*	1/3	2/3	0.3423	0.0414 / 0.959	2.63
Mn3 / Bi3	2*d*	1/3	2/3	0.0860	0.035 / 0.965	2.51
Te1	2*d*	1/3	2/3	0.5680	1	2.54
Te2	2*c*	0	0	0.2703	1	2.38
Te3	2*d*	1/3	2/3	0.8413	1	2.34
Te4	1a	0	0	0	1	2.12

Table S3: Wyckoff positions and atomic parameters (coordinates *x y z*, site occupancy factors *s.o.f.* and isotropic displacement parameters B_{eq}, all from single-crystal data and not further refined) used in the Rietveld refinement of $Mn_{0.81}Bi_{6.13}Te_{10}$.

Atom	Wyck.	x	y	z	s. o. f.	B_{eq}
Mn1/Bi1/□	3*a*	0	0	0	0.634 / 0.275 / 0.09	1.79
Mn2/Bi2	6*c*	0	0	0.29647	0.017 / 0.983	1.92
Mn3/Bi3	6*c*	0	0	0.23671	0.015 / 0.985	1.79
Mn4/Bi4	6*c*	0	0	0.47010	0.014 / 0.986	1.80
Te1	6*c*	0	0	0.34922	1	1.77
Te2	6*c*	0	0	0.05365	1	1.61
Te3	6*c*	0	0	0.41290	1	1.55
Te4	6*c*	0	0	0.11658	1	1.38
Te5	6*c*	0	0	0.17957	1	1.54

Table S4: Lattice parameters of $Mn_{1-x}□_{x/3}Bi_{4+2x/3}Te_7$ with x = 0.15, 0.167 and 0.2 from Rietveld refinements compared with single crystal data of $Mn_{0.85}□_{0.05}Bi_{4.10}Te_7$.

nominal composition	*a* (in Å)	*c* (in Å)	R_{wp}
$Mn_{0.80}Bi_{4.13}Te_7$	4.3610(1)	23.792(2)	0.028
$Mn_{0.833}Bi_{4.11}Te_7$	4.3606(2)	23.794(2)	0.029
$Mn_{0.85}Bi_{4.10}Te_7$	4.3613(1)	23.794(2)	0.027
SCXRD $Mn_{0.85}Bi_{4.10}Te_7$	4.3591(3)	23.769(2)	0.033 (*R*1 for I > 2σ(I))
$GeBi_4Te_7$-type phase in a heterogeneous sample with nominal composition $MnBi_6Te_{10}$	4.3612(6)	23.769(4)	0.025

Table S5: SEM-EDX results for samples with the nominal compositions $Mn_{0.85}Bi_{4.10}Te_7$ and $Mn_{0.81}Bi_{6.13}Te_{10}$ (data averaged from 7-8 point measurements), compared with the nominal compositions $MnBi_4Te_7$ and $MnBi_6Te_{10}$, respectively.

nominal composition	at.-% measured (8 points)	at.-% calc. for $Mn_{0.85}Bi_{4.10}Te_7$	at.-% calc. for $MnBi_4Te_7$
$Mn_{0.85}Bi_{4.10}Te_7$	**Mn**: 6.6(6); **Bi**: 34.7(3); **Te**: 58.7(4)	**Mn**: 7.1; **Bi**: 34.3; **Te**: 58.6	**Mn**: 8.33; **Bi**: 33.33; **Te**: 58.33
	at.-% measured (7 points)	at.-% calc. for $Mn_{0.81}Bi_{6.13}Te_{10}$	at.-% calc. for $MnBi_6Te_{10}$
$Mn_{0.81}Bi_{6.13}Te_{10}$	**Mn**: 4.5(3); **Bi**: 36.5(5); **Te**: 59.1(5)	**Mn**: 4.78; **Bi**: 36.19; **Te**: 59.03	**Mn**: 5.9; **Bi**: 35.3; **Te**: 58.8

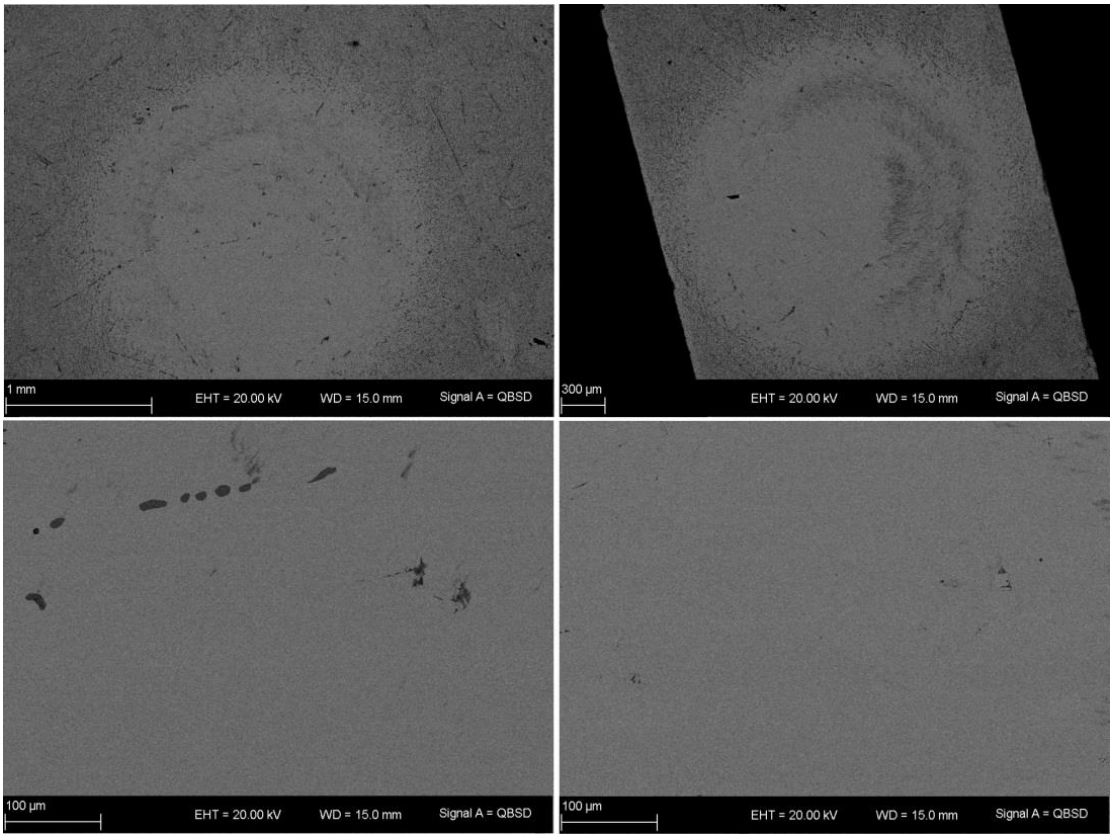

Figure S4: SEM images (backscattered electrons) of samples with the nominal compositions $Mn_{0.85}Bi_{4.10}Te_7$ (left) and $Mn_{0.81}Bi_{6.13}Te_{10}$ (right); the minor phase (black spots, bottom left) corresponds to a manganese telluride; the main phase (gray) to $Mn_{0.85}Bi_{4.10}Te_7$ (the influence of the minor phase on the composition is negligible) and $Mn_{0.81}Bi_{6.13}Te_{10}$, respectively.

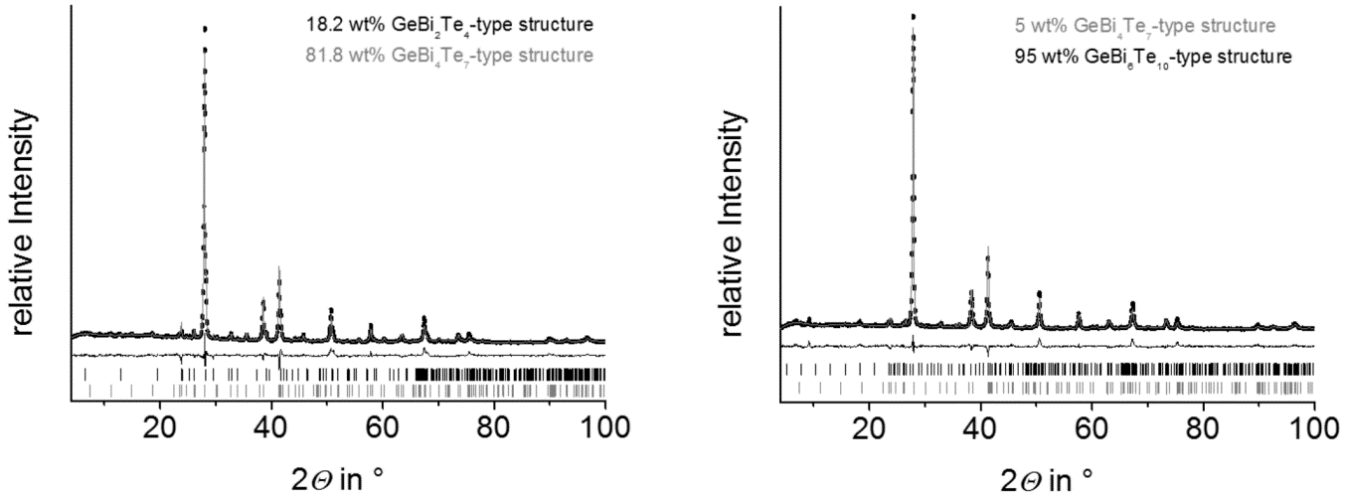

Figure S5: PXRD pattern of samples with the nominal compositions $Mn_{0.89}Bi_{4.11}Te_7$ (left) and $Mn_{0.85}Bi_{6.15}Te_{10}$ (right); Rietveld refinements taking into account structure models for $Mn_{0.85}Bi_{4.10}Te_7$ ($GeBi_4Te_7$-type structure, section 3.3), $Mn_{0.73}Bi_{6.18}Te_{10}$ ($GeBi_6Te_{10}$-type structure, section 3.3) and $Mn_{0.85}Bi_{2.1}Te_4$ [Zeugner, A.; Nietschke, F.; Wolter A. U. B.; Gaß, S.; Vidal, R. C.; Peixoto, T. R. F.; Pohl, D.; Damm, C.; Lubk, A.; Hentrich, R.; Moser, S. K.; Fornari, C.; Min, C. H., Schatz, S.; Kißner, K.; Ünzelmann, M.; Kaiser, M.; Scaravaggi, F. Rellinghaus, B.; Nielsch, K.; Heß, C.; Büchner, B.; Reinert, F.; Bentmann, H.; Oeckler, O.; Doert, T.; Ruck, M.; Isaeva, A. Chemical Aspects of the Antiferromagnetic Topological Insulator $MnBi_2Te_4$; available at arxiv.org/abs/1812.03106] based on SCXRD refinements; sum of calculated patterns light gray and experimental data as black points; difference plot (gray) and reflection markers below, gray markers for $GeBi_4Te_7$-type structure, black markers $GeBi_6Te_{10}$-type structure (right) and $GeBi_2Te_4$-type structure (left).

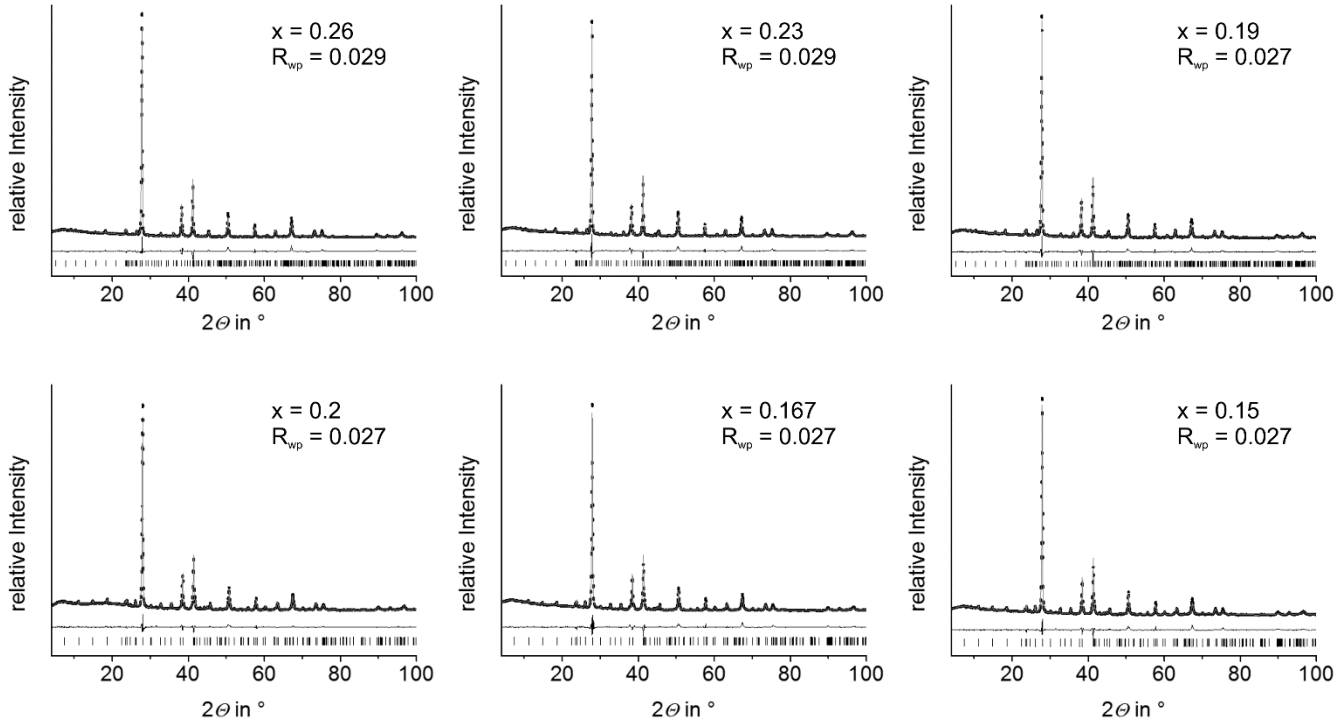

Figure S6: PXRD patterns of samples $Mn_{1-x}\square_{x/3}Bi_{6+2x/3}Te_{10}$ with x = 0.19, 0.23 and 0.26 (top row) and $Mn_{1-x}\square_{x/3}Bi_{4+2x/3}Te_7$ with x = 0.15, 0.167 and 0.2 (bottom row); Rietveld refinements taking into account structure models for $Mn_{0.85}Bi_{4.10}Te_7$ ($GeBi_4Te_7$ type) and $Mn_{0.73}Bi_{6.18}Te_{10}$ ($GeBi_6Te_{10}$ type) based on SCXRD (section 3.3); difference plots (gray), sum of calculated patterns light gray, experimental data as black points; reflection markers: black lines for $GeBi_4Te_7$ type (top) and $GeBi_6Te_{10}$ type (bottom), respectively.

Table S6: SEM-EDX data of $Mn_{1-x}\square_{x/3}Bi_{4+2x/3}Te_7$ with x = 0.15, 0.167 and 0.2 (top) and $Mn_{1-x}\square_{x/3}Bi_{6+2x/3}Te_{10}$ with x = 0.19, 0.23 and 0.26 (bottom) (averaged from eight point measurements) compared with the nominal composition $MnBi_4Te_7$ and $MnBi_6Te_{10}$.

Composition	at.-% measured	at.-% calculated (nominal)	at.-% calculated for $MnBi_4Te_7$
$Mn_{0.80}Bi_{4.13}Te_7$ (x = 0.2)	**Mn**: 6.5(5) **Bi**: 34.2(7) **Te**: 59.3(7)	**Mn**: 6.7 **Bi**: 34.6 **Te**: 58.7	**Mn**: 8.3 **Bi**: 33.3 **Te**: 58.3
$Mn_{0.833}Bi_{4.11}Te_7$ (x = 0.167)	**Mn**: 6.7(5) **Bi**: 34.6(5) **Te**: 58.7(5)	**Mn**: 7.0 **Bi**: 34.4 **Te**: 58.6	**Mn**: 8.3 **Bi**: 33.3 **Te**: 58.3
$Mn_{0.85}Bi_{4.10}Te_7$ (x = 0.15)	**Mn**: 6.6(6); **Bi**: 34.7(3); **Te**: 58.7(4)	**Mn**: 7.1; **Bi**: 34.3; **Te**: 58.6	**Mn**: 8.3 **Bi**: 33.3 **Te**: 58.3

Compositon	at.-% measured	at.-% calculated (nominal)	at.-% calculated for $MnBi_6Te_{10}$
$Mn_{0.74}Bi_{6.18}Te_{10}$ (x = 0.26)	**Mn**: 4.2(7); **Bi**: 36.5(4); **Te**: 59.4(4)	**Mn**: 4.4 **Bi**: 36.5 **Te**: 59.1	**Mn**: 5.9 **Bi**: 35.3 **Te**: 58.8
$Mn_{0.77}Bi_{6.15}Te_{10}$ (x = 0.23)	**Mn**: 4.5(6); **Bi**: 36.4(4); **Te**: 59.2(7)	**Mn**: 4.5 **Bi**: 36.4 **Te**: 59.1	**Mn**: 5.9 **Bi**: 35.3 **Te**: 58.8
$Mn_{0.81}Bi_{6.13}Te_{10}$ (x = 0.19)	**Mn**: 4.5(3); **Bi**: 36.5(5); **Te**: 59.1(5)	**Mn**: 4.8; **Bi**: 36.2; **Te**: 59.0	**Mn**: 5.9 **Bi**: 35.3 **Te**: 58.8

Table S7: Lattice parameters of $Mn_{1-x}\square_{x/3}Bi_{6+2x/3}Te_{10}$ with x = 0.19, 0.23 and 0.26 from Rietveld refinements compared with single-crystal data of $Mn_{0.73}\square_{0.09}Bi_{6.18}Te_{10}$.

nominal composition	*a* (in Å)	*c* (in Å)	R_{wp}
$Mn_{0.74}Bi_{6.18}Te_{10}$	4.3739(1)	101.818(8)	0.027
$Mn_{0.77}Bi_{6.15}Te_{10}$	4.3697(2)	101.863(8)	0.027
$Mn_{0.81}Bi_{6.13}Te_{10}$	4.3694(1)	101.870(7)	0.030
SCXRD $Mn_{0.73}Bi_{6.18}Te_{10}$	4.3698(3)	101.829(8)	0.0303 (*R*1 for I > 2σ(I))

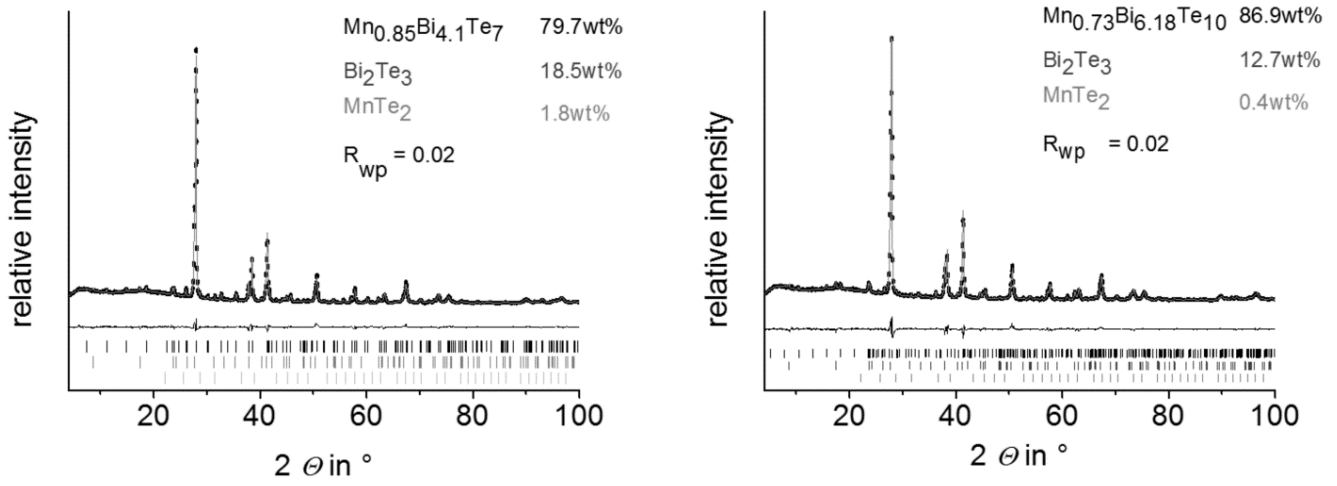

Figure S7: PXRD for samples with the nominal compositions $Mn_{0.85}Bi_{4.10}Te_7$ (left) and $Mn_{0.81}Bi_{6.13}Te_{10}$ (right) after thermoelectric characterization; Rietveld refinements taking into account structure models for $Mn_{0.85}Bi_{4.10}Te_7$ ($GeBi_4Te_7$ type), $Mn_{0.73}Bi_{6.18}Te_{10}$ ($GeBi_6Te_{10}$ type) based on SCXRD (section 3.3), for Bi_2Te_3 [Atuchin, V. V.; Gavrilova, T. A.; Kokh, K. A.; Kuratieva, N.V.; Pervukhina, N.B.; Surovtsev, N. V. *Solid State Commun.* 2012, *152*, 1119–1122] and for $MnTe_2$ (FeS_2-type structure, space group $Pa\bar{3}$) [Fjellvåg, H.; Kjekshus, A.; Chattopadhyay, T.; Hochheimer, H. D.; Hönle, W.; von Schnering, H. G. *Phys. Lett.* 1985, *112A*, 411–413]; experimental data (black points), refined curve (gray), difference plot (black) and reflection positions: black $GeBi_4Te_7$ type (left) and $GeBi_6Te_{10}$ type (right), respectively, dark gray Bi_2Te_3 type and light gray $MnTe_2$.

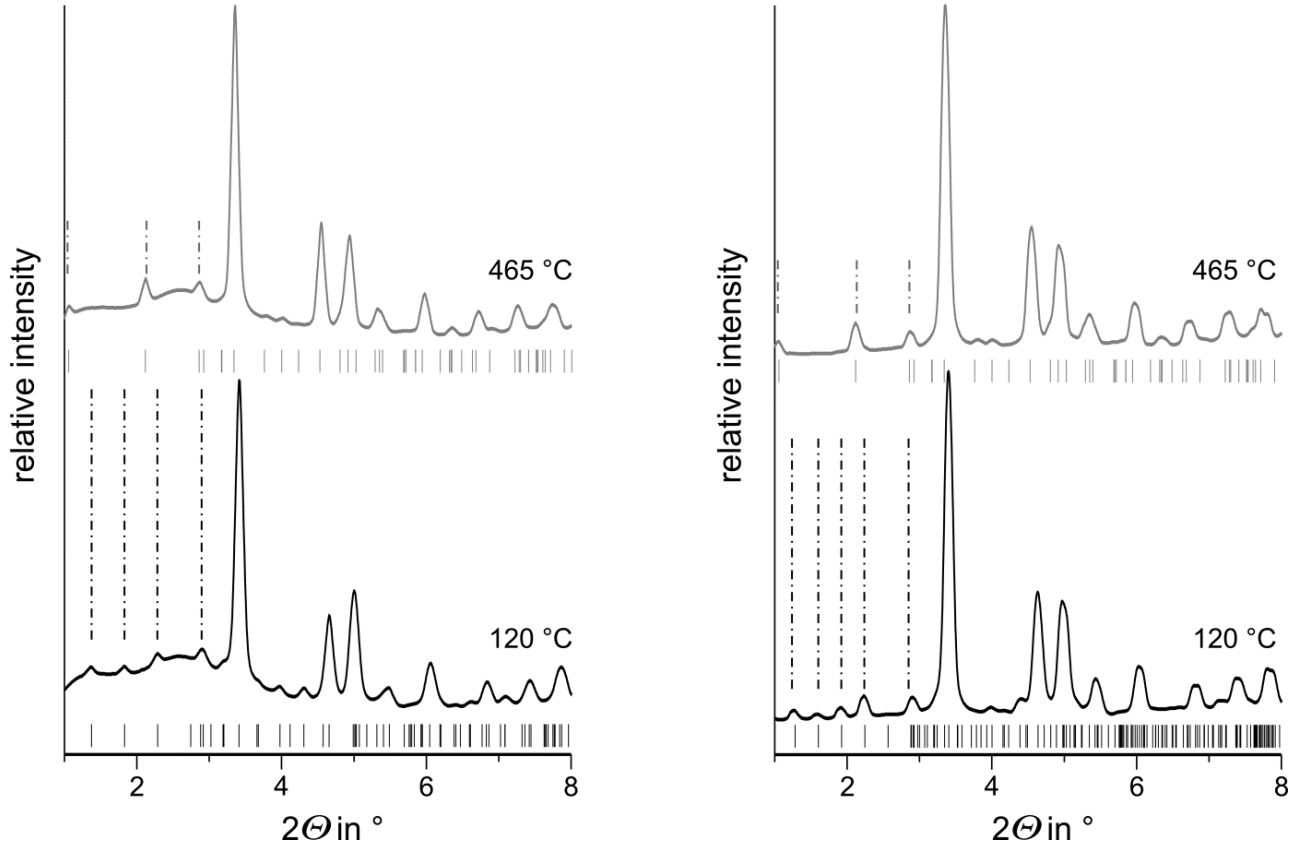

Figure S8: PXRD patterns (taken from Fig. 2, λ = 0.18972 Å) of $Mn_{0.85}Bi_{4.10}Te_7$ (left) and $Mn_{0.81}Bi_{6.13}Te_{10}$ (right) at 120 °C (black curve) and 465 °C (gray curve; Bi_2Te_3 type resulting from decomposition); vertical black lines and dashed black lines indicate the reflection positions of $GeBi_4Te_7$-type structure (left) and of $GeBi_6Te_{10}$-type structure (right), respectively; vertical gray lines and gray dashed lines indicate reflection positons of a Bi_2Te_3-type structure; note that the strongest reflections may easily be confused with each other.

Table S8: Signals of $Mn_{0.85}Bi_{4.10}Te_7$ in the DSC experiment and possible assignments.

Run	**Signal**	**T_{peak} / °C**	**possible assignment**
1st heating	shoulder of 1		melting of Bi_2Te_3
	1	590.2	melting of $Mn_{0.85}Bi_{4.10}Te_7$
	2	598.2	melting of Mn_2BiTe_4
1st cooling	1	588.7	solidification of Mn_2BiTe_4
	2	584.5	solidification of $Mn_{0.85}Bi_{4.10}Te_7$
	3	580.5	solidification of Bi_2Te_3
2nd heating	1	589.2	melting of Bi_2Te_3
	1‘	590.5	melting of $Mn_{0.85}Bi_{4.10}Te_7$
	2	596.5	melting of Mn_2BiTe_4
2nd cooling	1	588.7	solidification of Mn_2BiTe_4
	2	584.5	solidification of $Mn_{0.85}Bi_{4.10}Te_7$
	3	580.5	solidification of Bi_2Te_3

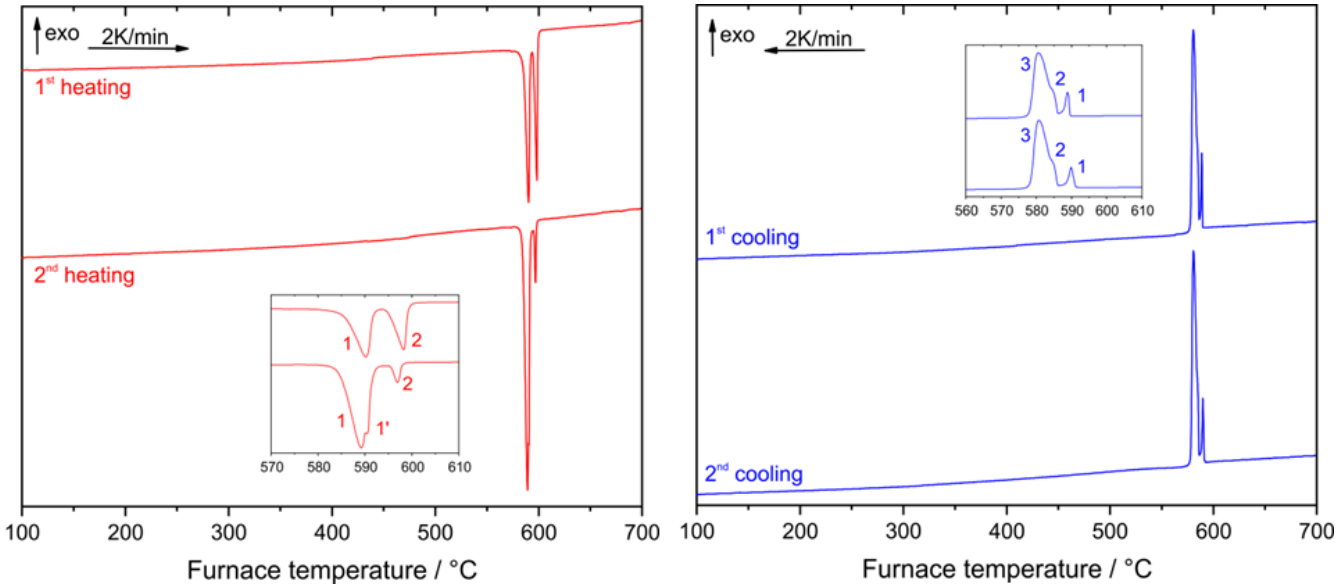

Figure S9: DSC experiments (two heating–cooling cycles from 100-700 °C) for $Mn_{0.85}Bi_{4.10}Te_7$.

Table S9: Signals of $Mn_{0.81}Bi_{6.13}Te_{10}$ DSC experiment and possible assignment.

Run	Signal	T_{peak} / °C	Possible assignment
1st heating	1	574.0	Melting Bi-rich Bi_xTe_y
	2	588.3	Melting $Mn_{0.81}Bi_{6.13}Te_{10}$
	3	590.0	Melting $Mn_{0.85}Bi_{4.10}Te_7$
	4	598.2	Melting Mn_2BiTe_4
1st cooling	1 (broad unstructured signal)		Bi_2Te_3 and Mn-poorer $□_{0.06}Mn_{0.81}Bi_{6.13}Te_{10}$ and $□_{0.05}Mn_{0.85}Bi_{4.10}Te_7$
2nd heating	1		Bi_2Te_3 and Mn-poorer $□_{0.06}Mn_{0.81}Bi_{6.13}Te_{10}$ and $□_{0.05}Mn_{0.85}Bi_{4.10}Te_7$
	2		Melting Mn_2BiTe_4
2nd cooling	1 (broad unstructured signal)		Bi_2Te_3 and Mn-poorer $□_{0.06}Mn_{0.81}Bi_{6.13}Te_{10}$ and $□_{0.05}Mn_{0.85}Bi_{4.10}Te_7$

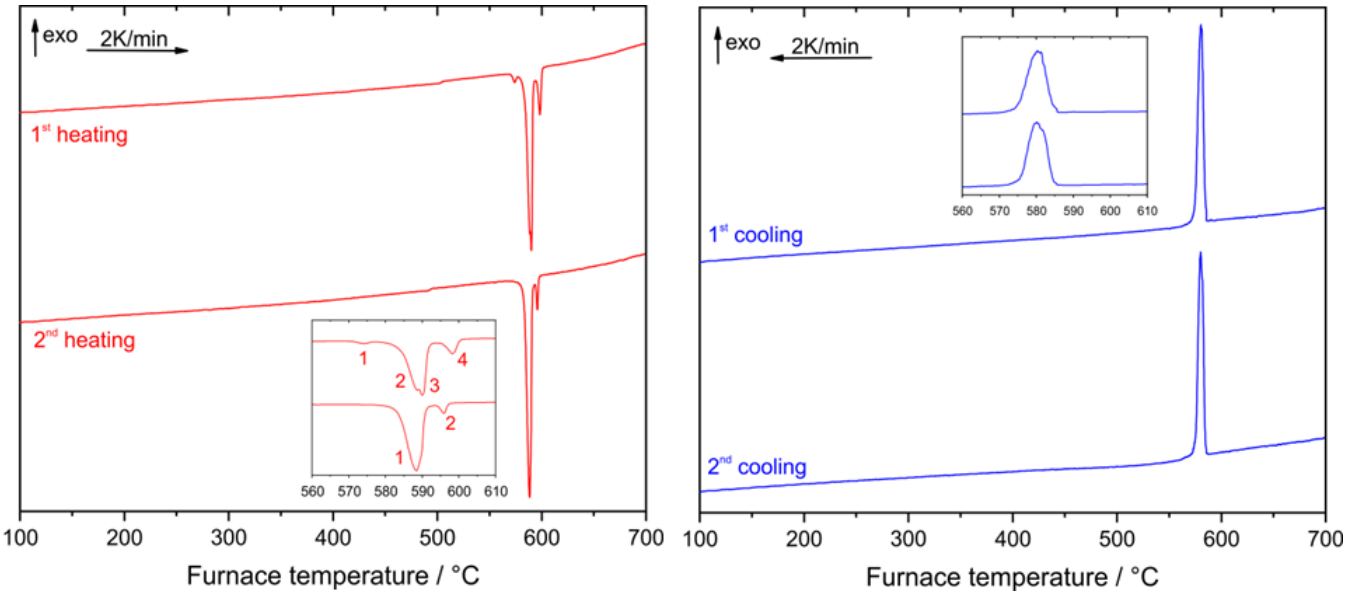

Figure S10: DSC experiments (two heating–cooling cycles from 100-700 °C) for $Mn_{0.81}Bi_{6.13}Te_{10.}$

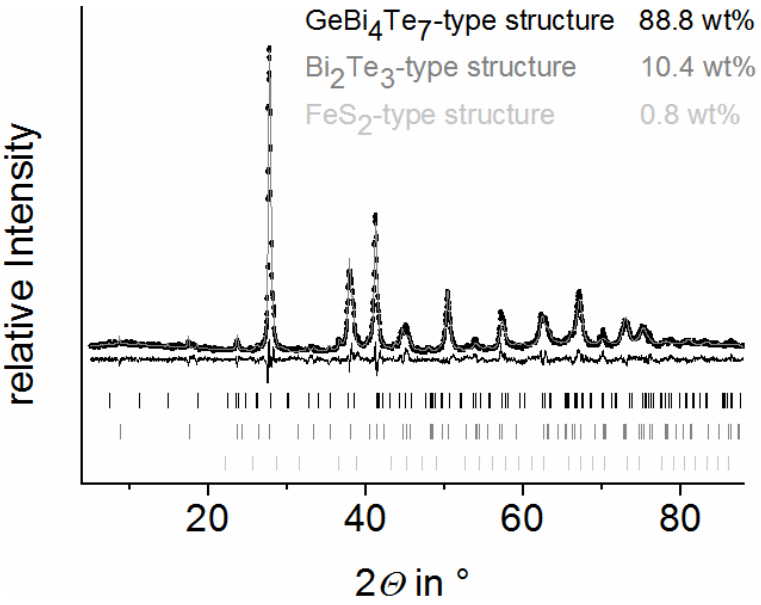

Figure S11: PXRD pattern of the decomposition product of a sample with the nominal composition $Mn_{0.85}Bi_{4.10}Te_7$ after DSC heating up to 400 °C; Rietveld refinements taking into account structure models for $Mn_{0.85}Bi_{4.10}Te_7$ ($GeBi_4Te_7$ type), $Mn_{0.73}Bi_{6.18}Te_{10}$ ($GeBi_6Te_{10}$ type) based on SCXRD refinements (section 3.3), for Bi_2Te_3 [Atuchin, V. V.; Gavrilova, T. A.; Kokh, K. A.; Kuratieva, N.V.; Pervukhina, N.B.; Surovtsev, N. V. *Solid State Commun.* **2012**, *152*, 1119–1122] and for $MnTe_2$ (FeS_2-type structure, space group $Pa\bar{3}$) [Fjellvåg, H.; Kjekshus, A.; Chattopadhyay, T.; Hochheimer, H. D.; Hönle, W.; von Schnering, H. G. Pressure induced phase transition in $MnTe_2$. *Phys. Lett.* **1985**, *112A*, 411–413]; experimental data (black points), refined curve (gray), difference plot (black) and reflection markers: black $GeBi_4Te_7$ type, dark gray Bi_2Te_3 type and light gray $MnTe_2$.

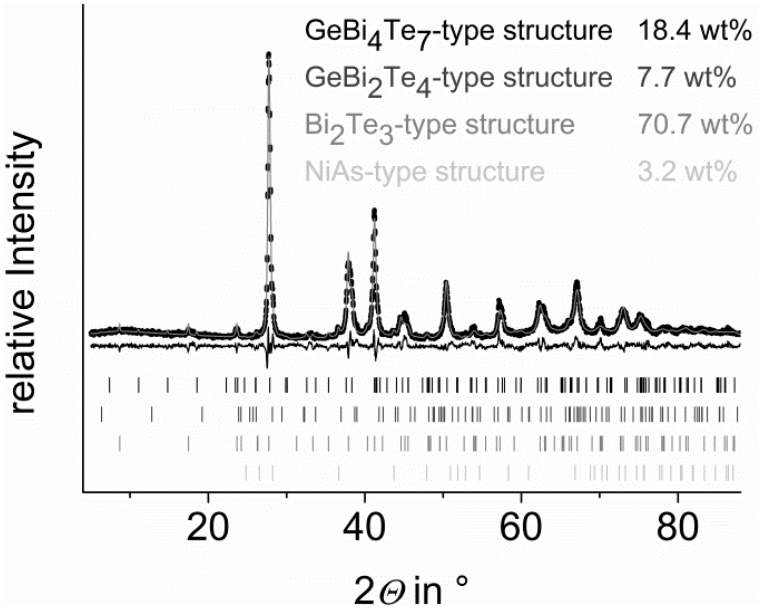

Figure S12: PXRD of the decomposition product of $Mn_{0.85}Bi_{4.10}Te_7$ after a DSC experiment with two consecutive cycles from RT up to 700 °C; Rietveld refinements taking into account structure models for $Mn_{0.85}Bi_{4.10}Te_7$ ($GeBi_4Te_7$-type structure, section 3.3), $Mn_{0.85}Bi_{2.1}Te_4$ [$GeBi_2Te_4$-type structure: [Zeugner, A.; Nietschke, F.; Wolter A. U. B.; Gaß, S.; Vidal, R. C.; Peixoto, T. R. F.; Pohl, D.; Damm, C.; Lubk, A.; Hentrich, R.; Moser, S. K.; Fornari, C.; Min, C. H., Schatz, S.; Kißner, K.; Ünzelmann, M.; Kaiser, M.; Scaravaggi, F. Rellinghaus, B.; Nielsch, K.; Heß, C.; Büchner, B.; Reinert, F.; Bentmann, H.; Oeckler, O.; Doert, T.; Ruck, M.; Isaeva, A. Chemical Aspects of the Antiferromagnetic Topological Insulator $MnBi_2Te_4$; available at arxiv.org/abs/1812.03106]; experimental data (black points), for Bi_2Te_3 [Atuchin, V. V.; Gavrilova, T. A.; Kokh, K. A.; Kuratieva, N.V.; Pervukhina, N.B.; Surovtsev, N. V. *Solid State Commun.* **2012**, *152*, 1119–1122] and for MnTe (NiAs-type structure) [Efrem D'Sa, J.B.C.; Bhobe, P. A.; Riolkar, K. R.; Das, A.; Paranjpe, S. K.; Prabhu, R. B.; Sarode, P. R. *J. Magn. Magn. Mater.* **2005**, *285*, 267–271], refined curve (gray), difference plot (black) and reflection positions (black $GeBi_4Te_7$ type; dark gray $GeBi_2Te_4$ type, gray Bi_2Te_3 type and light gray NiAs-type structure of MnTe).

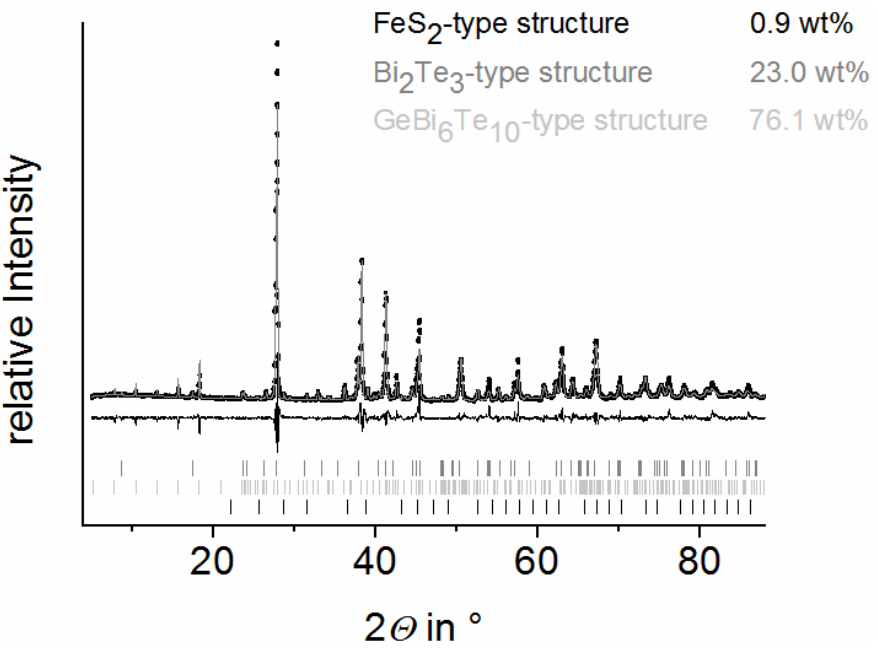

Figure S13: PXRD pattern of the decomposition product of $Mn_{0.81}Bi_{6.13}Te_{10}$ after DSC (heating up to 400 °C); Rietveld refinement taking into account structure models for $Mn_{0.85}Bi_{4.10}Te_7$ ($GeBi_4Te_7$-type structure), $Mn_{0.73}Bi_{6.18}Te_{10}$ ($GeBi_6Te_{10}$-type structure) based on SCXRD (section 3.3), for Bi_2Te_3 [Atuchin, V. V.; Gavrilova, T. A.; Kokh, K. A.; Kuratieva, N. V.; Pervukhina, N. B.; Surovtsev, N. V. *Solid State Commun.* **2012**, *152*, 1119–1122] and for $MnTe_2$ (FeS_2-type structure, space group $Pa\bar{3}$) [Fjellvåg, H.; Kjekshus, A.; Chattopadhyay, T.; Hochheimer, H. D.; Hönle, W.; von Schnering, H. G. *Phys. Lett.* **1985**, *112A*, 411–413]; experimental data (black points), refined curve (gray), difference plot (black) and reflection markers (black $GeBi_6Te_{10}$ type, dark gray Bi_2Te_3 type and light gray $MnTe_2$).

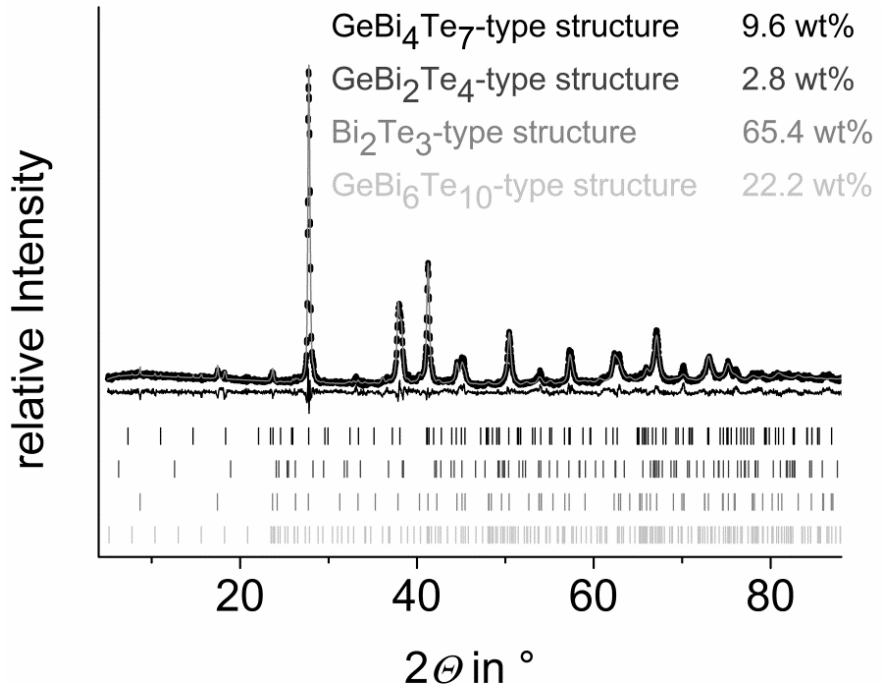

Figure S14: PXRD of the decomposition product of $Mn_{0.81}Bi_{6.13}Te_{10}$ after a DSC experiment with two consecutive cycles from RT up to 700 °C; Rietveld refinement taking into account structure models for $Mn_{0.85}Bi_{4.10}Te_7$ ($GeBi_4Te_7$ type), $Mn_{0.73}Bi_{6.18}Te_{10}$ ($GeBi_6Te_{10}$ type) based on SCXRD (section 3.3),and $Mn_{0.85}Bi_{2.1}Te_4$ [Zeugner, A.; Nietschke, F.; Wolter A. U. B.; Gaß, S.; Vidal, R. C.; Peixoto, T. R. F.; Pohl, D.; Damm, C.; Lubk, A.; Hentrich, R.; Moser, S. K.; Fornari, C.; Min, C. H., Schatz, S.; Kißner, K.; Ünzelmann, M.; Kaiser, M.; Scaravaggi, F. Rellinghaus, B.; Nielsch, K.; Heß, C.; Büchner, B.; Reinert, F.; Bentmann, H.; Oeckler, O.; Doert, T.; Ruck, M.; Isaeva, A. Chemical Aspects of the Antiferromagnetic Topological Insulator $MnBi_2Te_4$; available at arxiv.org/abs/1812.03106] and for Bi_2Te_3 [Atuchin, V. V.; Gavrilova, T. A.; Kokh, K. A.; Kuratieva, N. V.; Pervukhina, N. B.; Surovtsev, N. V. *Solid State Commun.* 2012, *152*, 1119–1122]; experimental data (black points), refined curve (gray), difference plot (black) and reflection markers (black $GeBi_4Te_7$ type; dark gray $GeBi_2Te_4$ type, gray Bi_2Te_3 type and light gray $GeBi_6Te_{10}$ type).

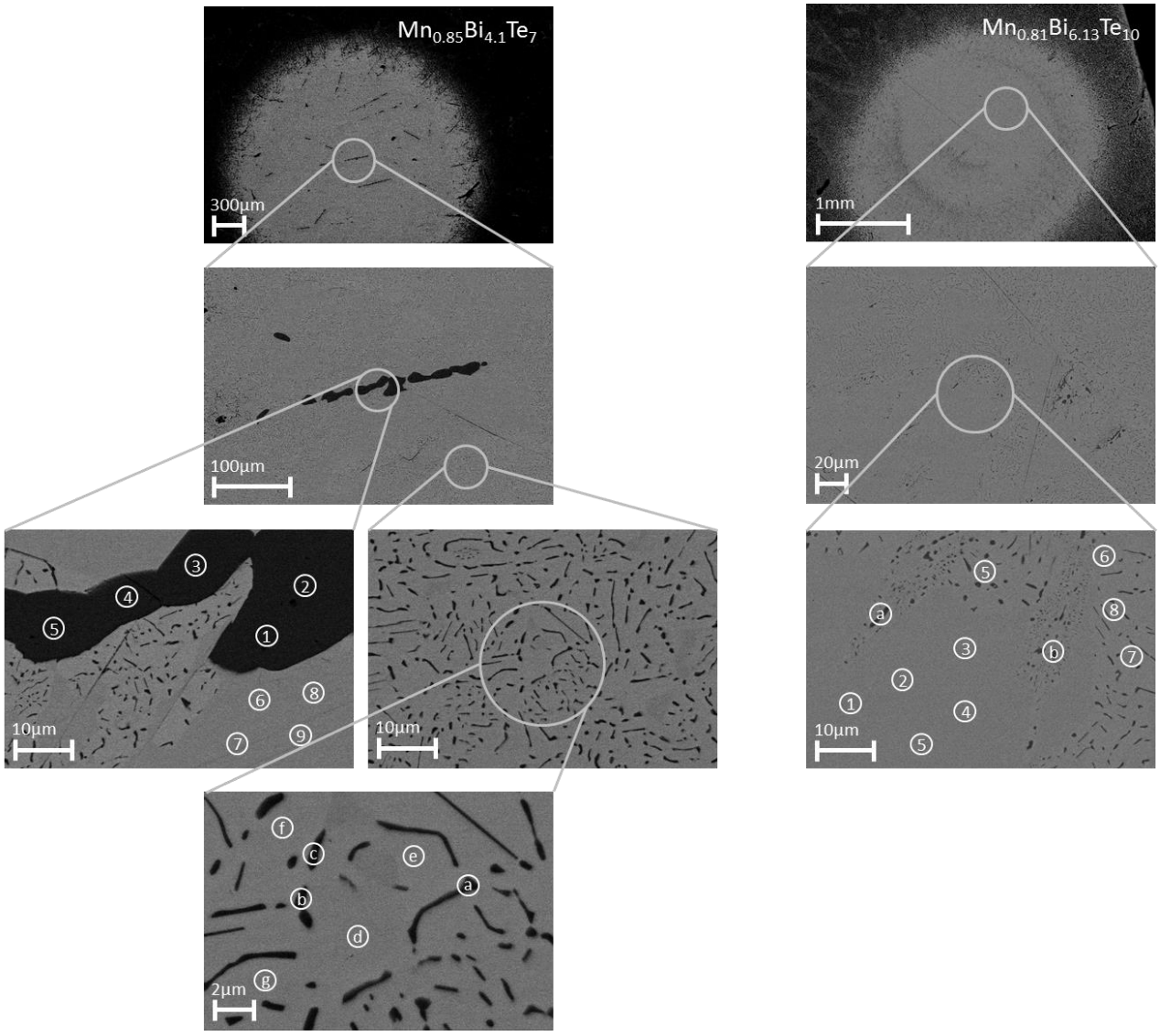

Figure S15: SEM images (backscattered electrons) after thermoelectric measurements (3 cycles; RT – 400 °C) of samples with the nominal composition $Mn_{0.85}Bi_{4.10}Te_7$ (left) and $Mn_{0.81}Bi_{6.13}Te_{10}$ (right) with increasing magnification from top to bottom; black areas (lines, spots) correspond to manganese tellurides and possibly other Mn-rich phases, light gray areas to Mn-doped Bi_2Te_3 and the dark gray main phase to $Mn_{0.85}Bi_{4.10}Te_7$ and $Mn_{0.81}Bi_{6.13}Te_{10}$, respectively; EDX results are given in Table S10.

Table S10: Results of SEM-EDX analyses (marked in Fig. S15) for samples with the nominal compositions $Mn_{0.85}Bi_{4.1}Te_7$ and $Mn_{0.81}Bi_{6.13}Te_{10}$ after thermoelectric measurements (3 cycles; RT-400 °C) taking into account formed precipitates; data averaged from 2-5 point measurements; the small size of the precipitates can result in large errors as surrounding matrix material may contribute to point measurements.

formula	**$Mn_{0.85}Bi_{4.10}Te_7$** (point 6-9)	**$MnTe_2$** (point 1-5)	**Bi_2Te_3** (point d-g)	**Mn-rich phase**(point a-c)
at.-% meas.	**Mn**: 6.4(10); **Bi**: 35.0(9); **Te**: 59.2(7)	**Mn**: 33.1(5); **Te**: 66.9(5)	**Mn**: 2.1(11); **Bi**: 37.7(10); **Te**: 60.23(6)	**Mn**: 19(2); **Bi**: 19(2); **Te**: 62.6(1)
at.-% calc.	**Mn**: 7.1; **Bi**: 34.3; **Te**: 58.6	**Mn**: 33.3; **Te**: 66.7	**Bi**: 40; **Te**: 60	"$MnTe_2$ + Bi_2Te_3"
formula	**$Mn_{0.81}Bi_{6.13}Te_{10}$** (1-5)		**Bi_2Te_3** (6-9)	**Mn-rich phase** (a-b)
at.-% meas.	**Mn**: 4.6(3); **Bi**: 36.2(5); **Te**: 59.2(5)		**Mn**: 1.7(6); **Bi**: 38.2(8); **Te**: 60.2(12)	**Mn**: 23(3); **Bi**: 13(2); **Te**: 64(2)
at.-% calc.	**Mn**: 4.78; **Bi**: 36.19; **Te**: 59.03		**Bi**: 40; **Te**: 60	"$MnTe_2$ + Bi_2Te_3"

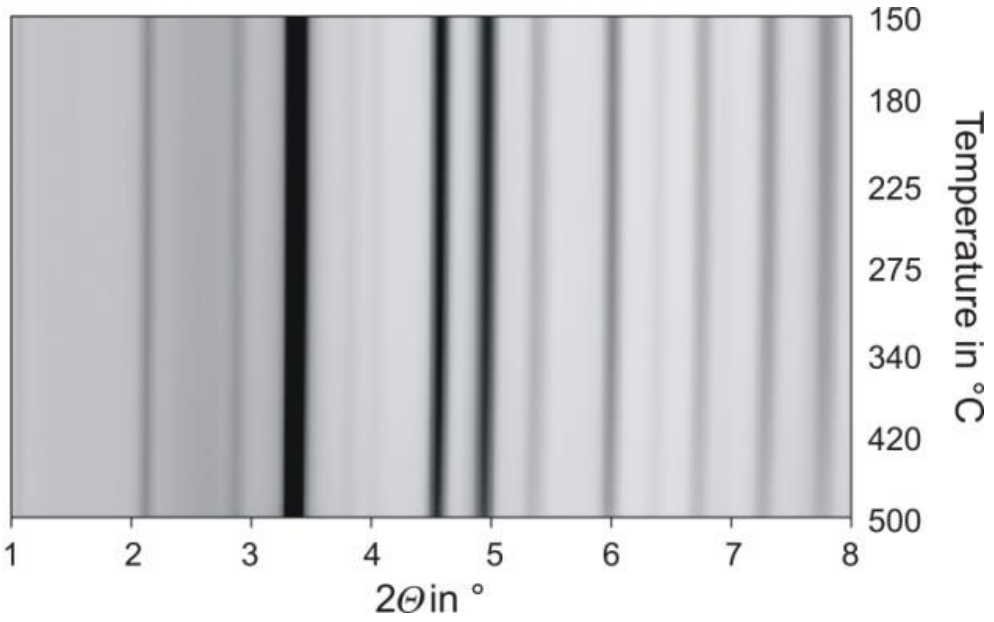

Figure S16: Temperature-dependent PXRD patterns of $Mn_{0.85}Bi_{4.10}Te_7$ during cooling (decomposition into a Bi_2Te_3-like structure took place during heating): the starting materials were not regained during cooling and the Bi_2Te_3-like structure remains (λ = 0.18972 Å, synchrotron radiation).

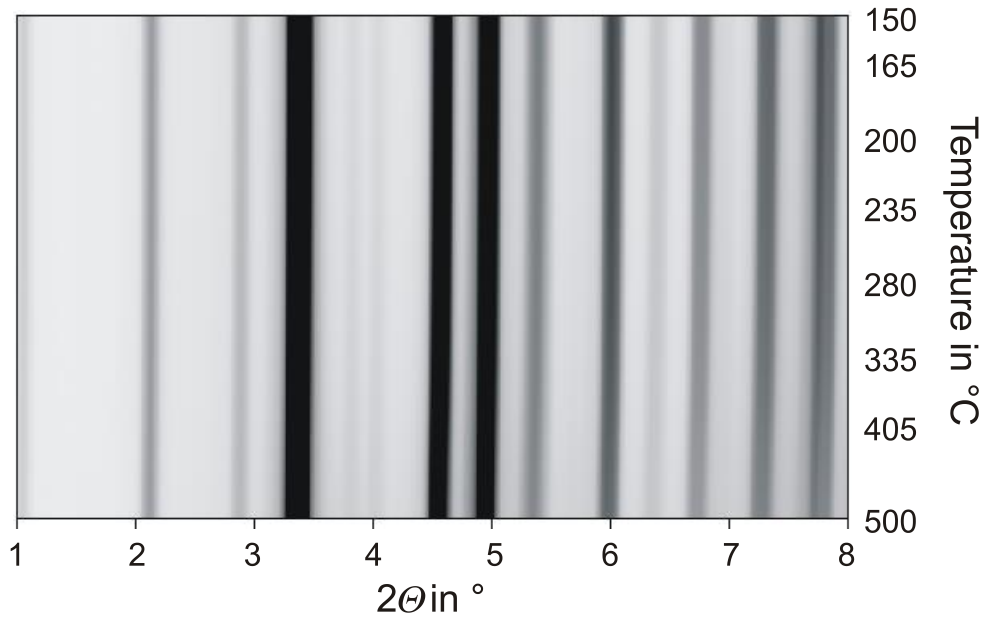

Figure S17: Temperature-dependent PXRD patterns of $Mn_{0.81}Bi_{6.13}Te_{10}$ during cooling (decomposition into a Bi_2Te_3-like structure took place during heating): the starting materials were not regained during cooling and the Bi_2Te_3-like structure remains (λ = 0.18972 Å, synchrotron radiation).

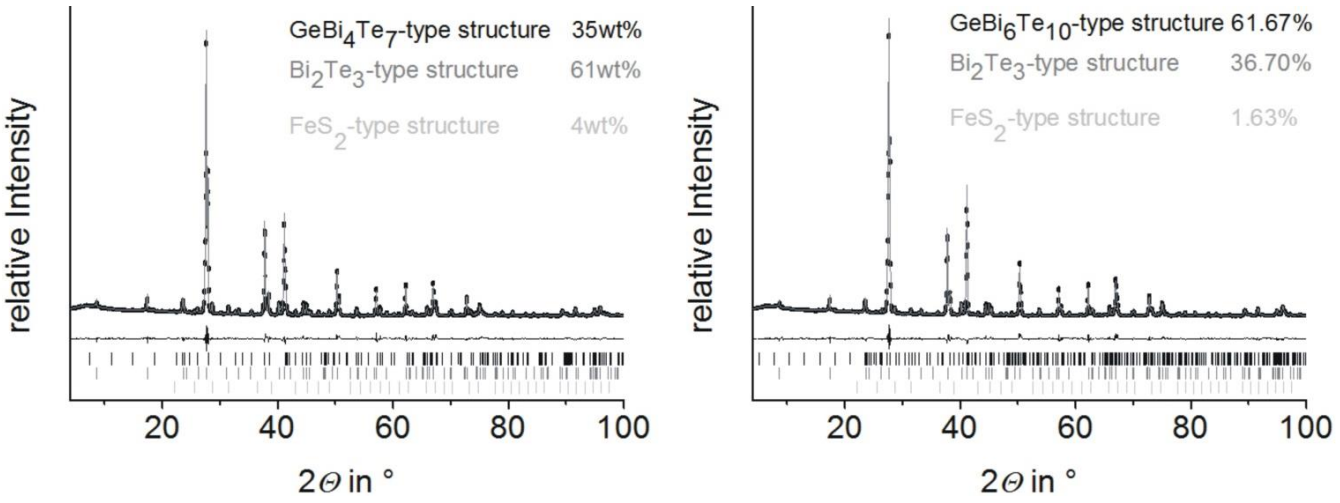

Figure S18: PXRD patterns of the decomposition products of $Mn_{0.85}Bi_{4.15}Te_7$ (left) and $Mn_{0.81}Bi_{6.13}Te_{10}$ (right) after 1d at 300 °C; Rietveld refinements taking into account structure models for $Mn_{0.85}Bi_{4.10}Te_7$ ($GeBi_4Te_7$ type), $Mn_{0.73}Bi_{6.18}Te_{10}$ ($GeBi_6Te_{10}$ type) based on SCXRD data (section 3.3), for Bi_2Te_3 [Atuchin, V. V.; Gavrilova, T. A.; Kokh, K. A.; Kuratieva, N. V.; Pervukhina, N. B.; Surovtsev, N. V. *Solid State Commun.* **2012**, *152*, 1119–1122] and for $MnTe_2$ (FeS_2-type structure, space group $Pa\bar{3}$) [Fjellvåg, H.; Kjekshus, A.; Chattopadhyay, T.; Hochheimer, H. D.; Hönle, W.; von Schnering, H. G. *Phys. Lett.* **1985**, *112A*, 411–413]; experimental data (black points), refined curve (gray), difference plot (black) and reflection markers black $GeBi_4Te_7$ type (left) or $GeBi_6Te_{10}$ type (right), dark gray Bi_2Te_3 type and light gray $MnTe_2$).

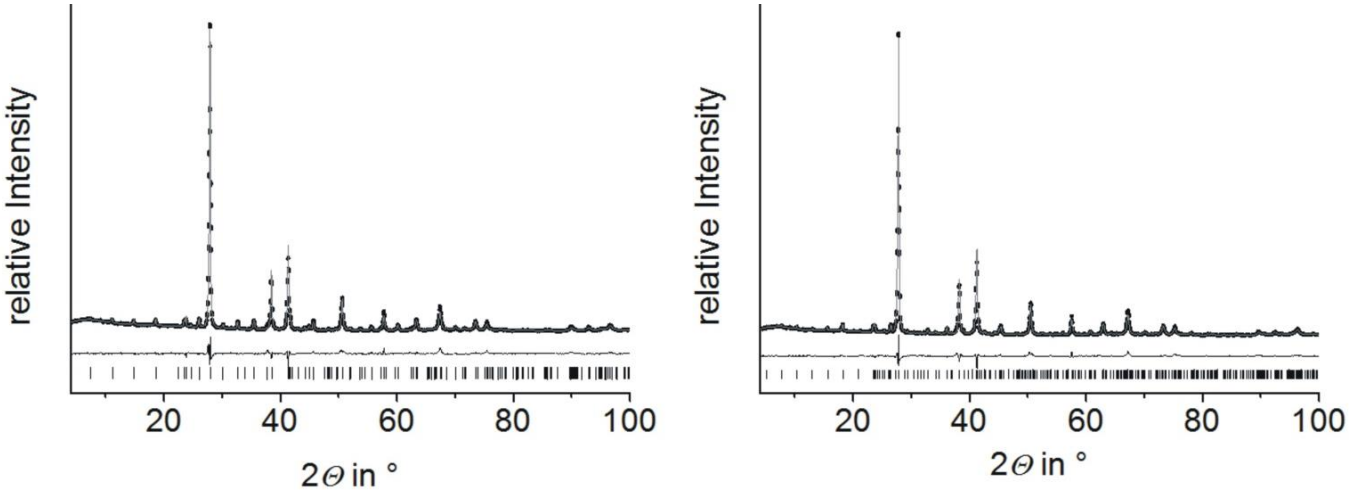

Figure S19: The decomposition products of Figure S18 were again treated like during the initial melt synthesis (section 2) and result in phase pure samples again: $Mn_{0.85}Bi_{4.10}Te_7$ (left) and $Mn_{0.81}Bi_{6.13}Te_{10}$ (right); Rietveld refinements taking into account structure models for $Mn_{0.85}Bi_{4.10}Te_7$ ($GeBi_4Te_7$ type) and $Mn_{0.73}Bi_{6.18}Te_{10}$ ($GeBi_6Te_{10}$ type) based on SCXRD refinements (section 3.3); calculated patterns light gray, experimental data black points; difference plot (black) and reflection markers (black lines for $GeBi_4Te_7$ type and $GeBi_6Te_{10}$ type, respectively).

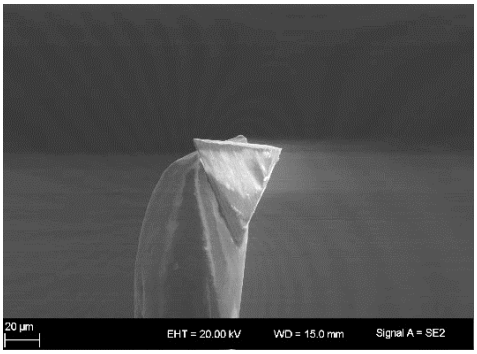

Figure S20: SEM SE image of the $Mn_{0.85}Bi_{4.10}Te_7$ single crystal used for structure analysis.

Table S11: SEM-EDX data of the $Mn_{0.85}Bi_{4.10}Te_7$ crystal used for structure analysis (averaged from five point measurements).

at.-% measured	at.-% calculated for $Mn_{0.85}Bi_{4.10}Te_7$	at.-% calculated for $MnBi_4Te_7$
Mn: 5.8(5); **Bi**: 35.9(5); **Te**: 58.3(3)	**Mn**: 7.1; **Bi**: 34.3; **Te**: 58.6	**Mn**: 8.33 **Bi**: 33.33 **Te**: 58.33

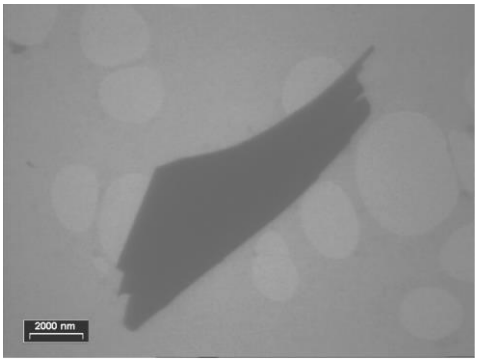

Figure S21: TEM image of the $Mn_{0.73}Bi_{6.18}Te_{10}$ single crystal used for structure analysis.

Table S12: TEM-EDX data of the $Mn_{0.73}Bi_{6.18}Te_{10}$ crystal used for structure analysis (averaged from two point measurements).

at.-% measured	at.-% calculated for $Mn_{0.73}Bi_{6.18}Te_{10}$	at.-% calculated for $MnBi_6Te_{10}$
Mn: 5.4(4); **Bi**: 36.4(4); **Te**: 58.2(2)	**Mn**: 4.3; **Bi**: 36.5; **Te**: 59.1	**Mn**: 5.9 **Bi**: 35.3 **Te**: 58.8

Table S13: Selected interatomic distances (in Å) for $Mn_{0.85}Bi_{2.10}Te_4$ [Zeugner, A.; Nietschke, F.; Wolter A. U. B.; Gaß, S.; Vidal, R. C.; Peixoto, T. R. F.; Pohl, D.; Damm, C.; Lubk, A.; Hentrich, R.; Moser, S. K.; Fornari, C.; Min, C. H., Schatz, S.; Kißner, K.; Ünzelmann, M.; Kaiser, M.; Scaravaggi, F. Rellinghaus, B.; Nielsch, K.; Heß, C.; Büchner, B.; Reinert, F.; Bentmann, H.; Oeckler, O.; Doert, T.; Ruck, M.; Isaeva, A. Chemical Aspects of the Antiferromagnetic Topological Insulator $MnBi_2Te_4$; available at arxiv.org/abs/1812.03106], Bi_2Te_3 [Mansour, A. N.; Wong-Ng, W.; Huang, W.: Tang, W.; Tompson, A.; Sharp, J. *J. Appl. Phys*. 2014, *116*, 083513] as well as $Mn_{0.85}Bi_{4.10}Te_7$ and $Mn_{0.73}Bi_{6.18}Te_{10}$ (this work).

$Mn_{0.73}Bi_{6.18}Te_{10}$	bond length in Å	**$Mn_{0.85}Bi_{4.10}Te_7$**	bond length in Å	**$Mn_{0.85}Bi_{2.1}Te_4$**	bond length in Å	**Bi_2Te_3**	bond length in Å
septuple layer		septuple layer		septuple layer			
Mn2/Bi2 – Te2	3.0473(5)	Mn2/Bi2 –Te2	3.0436(7)	Bi1/Mn1 –Te2	3.027(1)		
Mn2/Bi2 – Te1	3.3055(6)	Mn2/Bi2 –Te1	3.2987(9)	Bi1/Mn1 – Te1	3.291(1)		
Mn1/Bi1 – Te1	2.9969(4)	Mn1/Bi1 –Te1	2.9909(7)	Bi2/Mn2 –Te1	2.977(1)		
van der Waals gap		van der Waals gap		van der Waals gap		van der Waals gap	
Te2 ··· Te3	3.6516(5)	Te2 ··· Te3	3.6559(7)	Te2 ··· Te2	3.699(1)	Te2 – Te2	3.630
Te5 ··· Te5	3.6432(5)						
quintuple layers		quintuple layer		quintuple layer		quintuple layer	
Mn3/Bi3 – Te3	3.0628(5)	Mn3/Bi3 – Te3	3.0543(7)			Bi – Te2	3.067
Mn3/Bi3 – Te4	3.2395(5)	Mn3/Bi3 –Te4	3.2410(4)			Bi – Te1	3.254
Mn4/Bi4 – Te4	3.2536(5)						
Mn4/Bi4 – Te5	3.0594(5)						

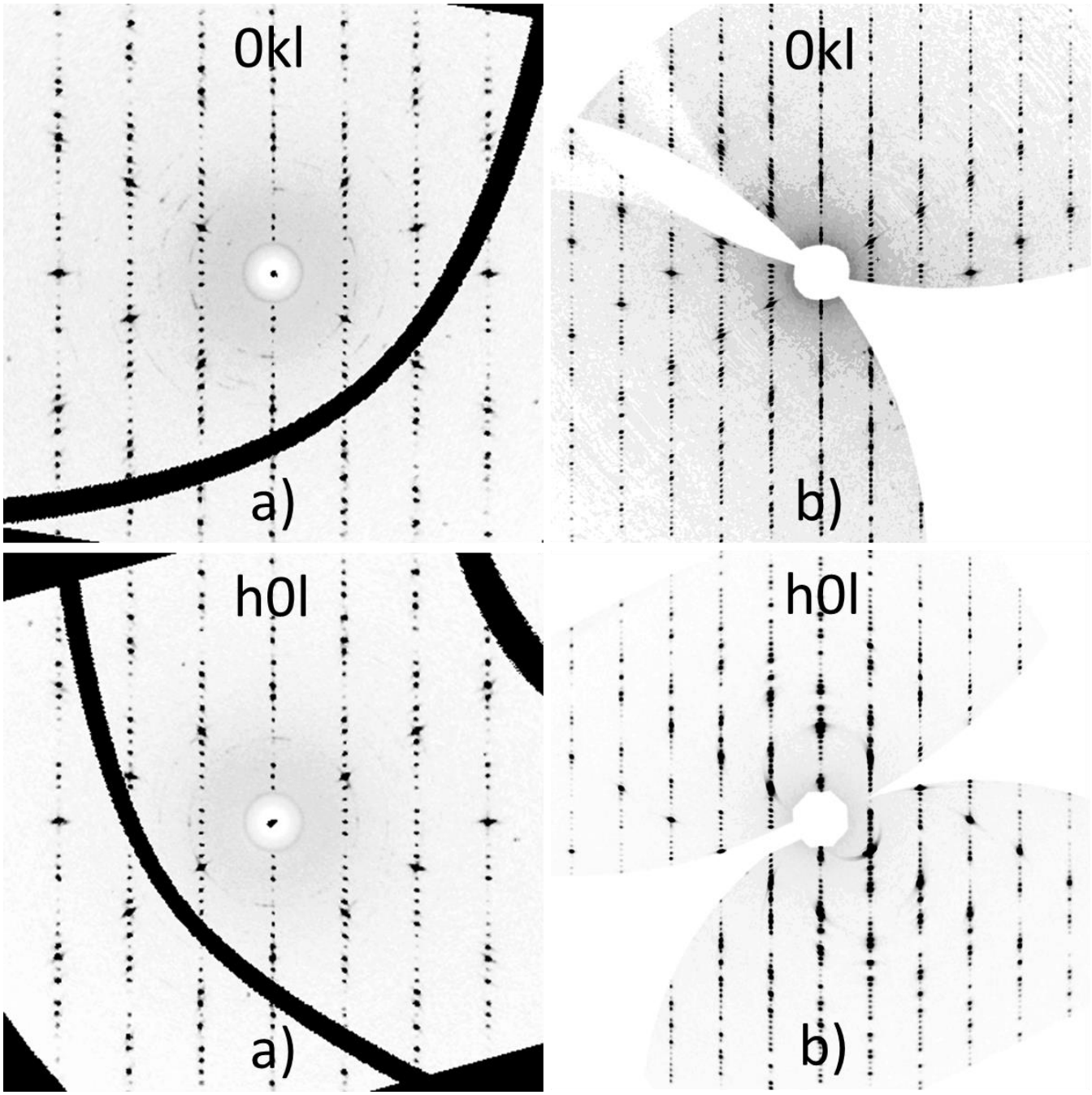

Figure S22: Reconstructed reciprocal lattice sections 0*kl* (top) and *h*0*l* (bottom) from the data of the crystals used for structure analysis: a) $Mn_{0.85}Bi_{4.10}Te_7$ single crystal ($GeBi_4Te_7$-type structure) and b) $Mn_{0.73}Bi_{6.18}Te_{10}$ single crystal ($GeBi_6Te_{10}$-type structure). No pronounced diffuse streaks, which would suggest stacking disorder, are visible in the experimental diffraction patterns of both crystals.

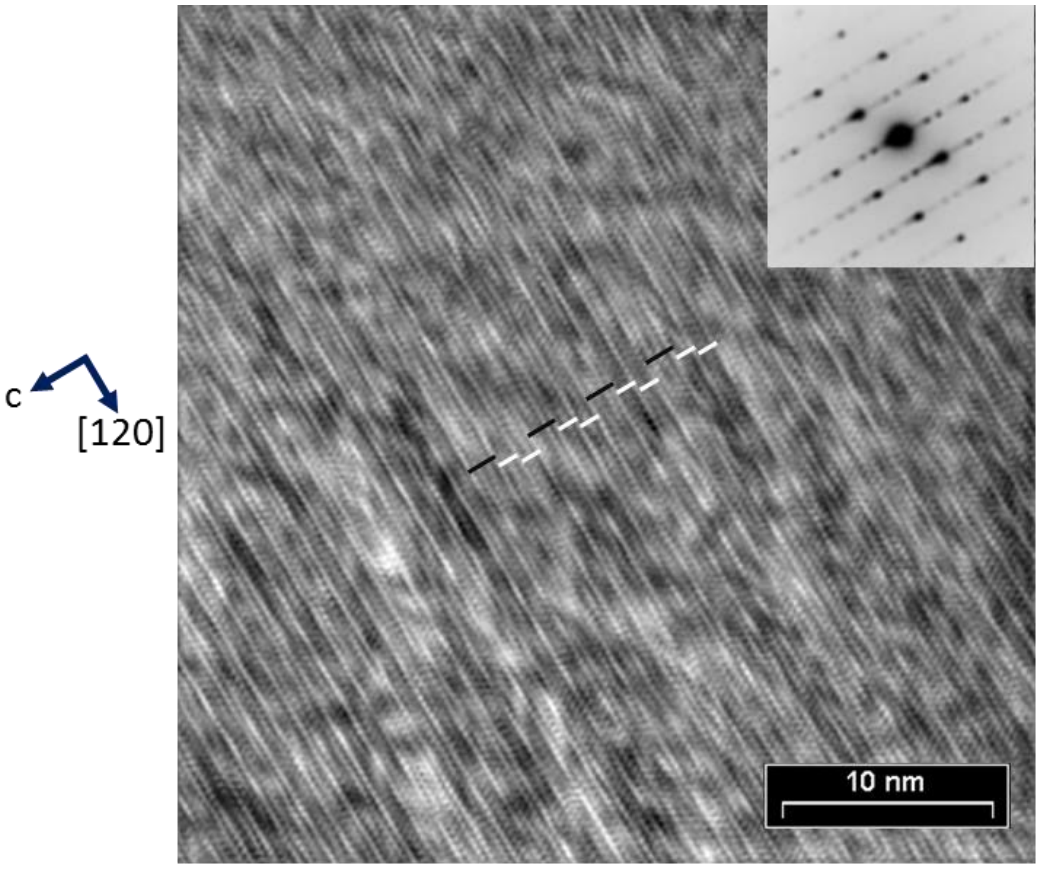

Figure S23: HRTEM image (zone axis [100], Fourier filtered) of manganese bismuth tellurides with $GeBi_6Te_{10}$ structure type (space group $R\bar{3}m$, a = 4.370 Å, c = 101.82 Å, Δf = -67 nm, t = 0.88 nm; beam semiconvergence 1.2 mrad, defocus spread 15 nm), with a corresponding SAED pattern in the upper right corner; in order to symbolize the long-range order, white bars symbolize quintuple Bi_2Te_3-like slab and black lines symbolize septuple layers characteristic of $MnBi_2Te_4$.

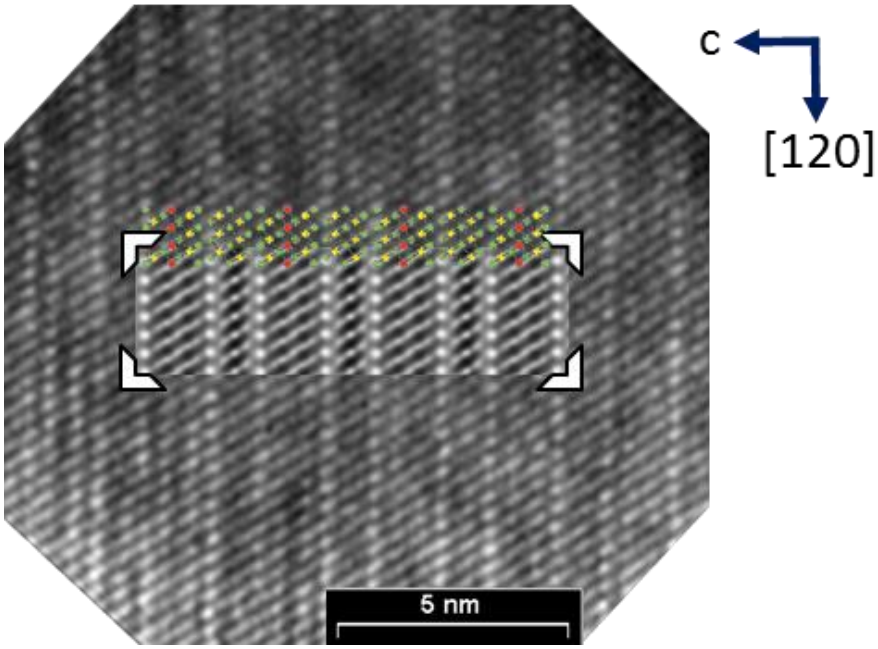

Figure 24: HRTEM image (zone axis [100]) of a manganese bismuth telluride with $GeBi_4Te_7$-type structure; inset: simulation based on single-crystal data of $Mn_{0.85}Bi_{4.10}Te_7$ (space group $P\bar{3}m1$, a = 4.359 Å, c = 23.77 Å, Δf = -85 nm, t = 8.36 nm; beam semiconvergence 1.2 mrad, defocus spread 15 nm); in the upper part of the simulation, the atom positions of the $GeBi_4Te_7$-type structure are illustrated (green = Te; yellow = Bi-rich cation position; red = Mn-rich cation position); for the exact cation distribution, including mixed sites, cf. Tables 2 and 4.

Modelling of transport properties and thermoelectric data

First, the electron chemical potential η was estimated from the measured Seebeck coefficient at a given temperature by numerical methods:

$$S(\eta) = \frac{k_B}{e}(2\frac{F_1(\eta)}{F_0(\eta)} - \eta)$$

with the Fermi integrals $F(\eta)$ being defined as:

$$F_x(\eta) = \int f\varepsilon^x d\varepsilon = \int \frac{\varepsilon^x d\varepsilon}{1 + \exp(\varepsilon - \eta)}$$

From η and the measured electrical conductivity σ, the intrinsic electrical conductivity σ_{E0} was calculated:

$$\sigma_{E_0} = \frac{\sigma}{\ln(1 + e^{\eta})}$$

Further, the phononic part of thermal conductivity κ_{ph} was calculated from the measured σ and thermal conductivity κ:

$$\kappa_{ph} = \kappa - L(\eta)\,\sigma\,T$$

with the Lorenz number $L(\eta)$ being calculated as:

$$L(\eta) = \frac{{k_B}^2}{e^2}\frac{3F_0(\eta)F_2(\eta) - 4F_1(\eta)^2}{F_0(\eta)^2}$$

The quality factor B was obtained from the following equation:

$$B = \left(\frac{k_B}{e}\right)^2 \frac{\sigma_{E_0}}{\kappa_{ph}} T$$

For a given B, η was varied in order to find the optimal doping level, obtaining ZT for different chemical potentials η (see chapter 3.6):

$$zT(\eta) = \frac{S^2(\eta)}{\frac{(k_B/e)^2}{B\ ln(1 + e^{\eta})} + L(\eta)}$$